Check for updates

Aortic haemodynamics and wall stress analysis following arch aneurysm repair using a single-branched endograft

Sampad Sengupta[1], Xun Yuan[2,3], Ludovica Maga[4,5], Selene Pirola[5], Christoph A. Nienaber[2,3] and Xiao Yun Xu[1]*

[1]Department of Chemical Engineering, Imperial College London, London, United Kingdom, [2]National Heart and Lung Institute, Faculty of Medicine, Imperial College London, London, United Kingdom, [3]Cardiology and Aortic Centre, Royal Brompton and Harefield Hospitals, Guy's and St Thomas' NHS Foundation Trust, London, United Kingdom, [4]Department of Electronics, Information and Bioengineering, Politecnico di Milano, Milan, Italy, [5]Department of Biomechanical Engineering, Delft University of Technology, Delft, Netherlands

Introduction: Thoracic endovascular aortic repair (TEVAR) of the arch is challenging given its complex geometry and the involvement of supra-aortic arteries. Different branched endografts have been designed for use in this region, but their haemodynamic performance and the risk for post-intervention complications are not yet clear. This study aims to examine aortic haemodynamics and biomechanical conditions following TVAR treatment of an aortic arch aneurysm with a two-component single-branched endograft.

Methods: Computational fluid dynamics and finite element analysis were applied to a patient-specific case at different stages: pre-intervention, post-intervention and follow-up. Physiologically accurate boundary conditions were used based on available clinical information.

Results: Computational results obtained from the post-intervention model confirmed technical success of the procedure in restoring normal flow to the arch. Simulations of the follow-up model, where boundary conditions were modified to reflect change in supra-aortic vessel perfusion observed on the follow-up scan, predicted normal flow patterns but high levels of wall stress (up to 1.3M MPa) and increased displacement forces in regions at risk of compromising device stability. This might have contributed to the suspected endoleaks or device migration identified at the final follow up.

Discussion: Our study demonstrated that detailed haemodynamic and biomechanical analysis can help identify possible causes for post-TEVAR complications in a patient-specific setting. Further refinement and validation of the computational workflow will allow personalised assessment to aid in surgical planning and clinical decision making.

KEYWORDS

TEVAR, endograft, aortic arch, computational fluid dynamics, finite element analysis

1. Introduction

An aortic aneurysm is a localised distention of the vessel wall, resulting in an abnormal and often permanent dilatation of the affected section of the aorta. Thoracic aortic aneurysms (TAAs) can arise in the ascending aorta, aortic arch, thoracic descending aorta, or the thoraco-abdominal regions of the aorta. Isolated arch aneurysms are less frequent but pose a significant challenge given the geometric complexity of the region,

especially the involvement of supra-aortic vessels that are responsible for supplying blood to the head and upper parts of the body. Insufficient blood perfusion to the arch branches can result in severe and often fatal consequences (1–3). The standard treatment option for arch aneurysm is open-chest surgery, with thoracic endovascular aortic repair (TEVAR) providing a minimally invasive alternative. Initially introduced for the treatment of abdominal aortic aneurysms, endovascular repair has now been extended to the thoracic aorta and arch. TEVAR offers several benefits to patients, including short post-operative time spent in the hospital and fast recovery (4–6).

Endografts used for TEVAR are designed to mimic a patient's anatomy as closely as possible. They can be branched or unbranched, depending on the zone of the aorta in which they are deployed. Improvements have been made to the design and deployment methods of endografts, yielding a remarkable decrease in mortality and morbidity rates of the repair procedure (4, 7). Branched or fenestrated stent-grafts are often used to ensure perfusion of blood to the supra-aortic vessels when implanted in the arch. Branched stent-grafts are conceptually more appealing than fenestrated devices as they are adaptable to a wide range of anatomical morphologies. Branched stent-grafts can be manufactured as either single- or multi-branched endografts with or without inner tunnels. These inner tunnels can be either antegrade or retrograde with antegrade tunnel branches tending to provide a smoother transition of flow into the arch branches as reported in previous computational studies (8). Single-branched stent-graft requires two bypass connections between the upper branches, e.g., bypass between the innominate artery and the left common carotid artery or between the left subclavian artery and the left common carotid, and thus may result in insufficient blood perfusion to the supra-aortic arteries as the entire flow is supplied by a single bridging stent. Double-branched endografts are developed for zone 0 deployment with two bridging stents connected to the innominate and left common carotid arteries (9, 10). The choice of endograft used lies with clinicians and is based on the treatment procedure, deployment zone, and other peri-operative factors.

Implanting an endovascular device will obviously change the flow within the repaired region, and it is of particular interest to gain more insights into the haemodynamic changes induced by the endograft (11, 12). *In vivo* examinations and clinical imaging alone cannot provide information on certain parameters of interest such as wall shear stress (WSS), forces exerted on the wall, and localised flow patterns. Previous studies have examined the performance of endografts in the aortic arch and their ability to perfuse the arch branches. For example, Zhu et al. (13) and Sengupta et al. (14) performed computational fluid dynamics (CFD) analysis of aortic flow after implantation of double-branched endografts in patients with arch aneurysms and noted improved flow patterns with increased WSS in the aortic arch. However, the presence of such inner branches can lead to disturbed flow in the region. In addition, arch endografts often involve occlusion of the native ostia of supra-aortic branches and peri-operative revascularisation procedures are required to

maintain perfusion to the arch branches (15). Left subclavian artery revascularisation, often through the left common carotid artery, can lead to increased flow in the remaining native vessels with increased peak flow velocity and higher displacement forces being exerted in the region (16, 17).

The influence of endografts on flow in the repaired aorta depends strongly on their design, and here the focus is on the effect of a single-branched device with no inner tunnel branches, suitable for zone 0 deployment to treat aortic arch pathologies. The device implanted in the patient included in this investigation is the Nexus™ Aortic Arch Stent Graft System developed by Endospan (Herzlia, Israel). As shown in **Figure 1**, it consists of a main module for the aortic arch and descending aorta with a side-branch for one supra-aortic vessel and a curved module for the ascending aorta that connects to the main module through a self-protecting sleeve (18). The device is suitable for implantation in zone 0 to zone 2 in the thoracic aorta and the branch emerging from the main module serves as an anchoring mechanism to hold the component in place. Being an "off the shelf" device, the length of each module and the diameters are chosen based on the application and anatomical features of the aorta being treated (19). The proximal end of the device has curved stent tips designed for atraumatic sealing in the ascending aorta and is meant to reduce pressure points on the outer curvature. The two modules overlap and have a radial force interlocking mechanism holding the separate components together in the ascending region.

This investigation aimed to examine the haemodynamic and biomechanical conditions of the aorta following TEVAR treatment for an aortic arch aneurysm with the Nexus™ device. We used patient-specific geometric models reconstructed from computed tomography (CT) scans acquired before and after the interventional procedure and at follow-up.

FIGURE 1
The NEXUS™ device selected for TEVAR, highlighting its features and different components.
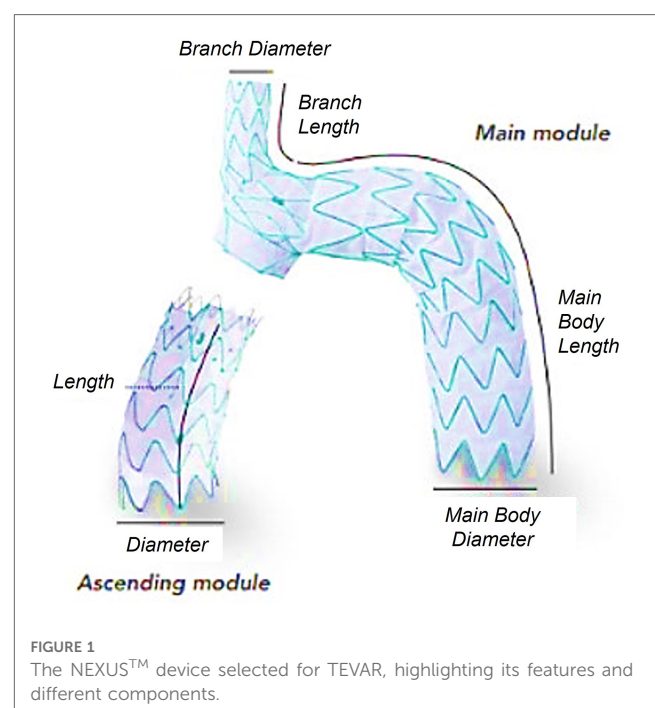
2. Materials and methods

2.1. Patient data

Clinical data and images were acquired from a patient with a large aneurysm arising from the inferior wall of the aortic arch. The patient underwent TEVAR with a single-branched Nexus™ device. **Figure 2** outlines the timeline of the case being studied, with reconstructions from clinical images showing the progression of the case. Ethical approval was obtained from the local Ethics Committee, and written consent was given by the patient.

The aneurysm, measuring $9.6 \times 6.0 \times 5.9$ cm in the aneurysmatic sac, led to compressions in the distal pulmonary vessels but there were no morphometric changes to the innominate artery (IA), left common carotid (LCC) artery and left subclavian artery (LSA). Pre-intervention CT images with measurements of diameters and distances at three different locations are shown in **Figure 3**.

The patient was treated with TEVAR using the Nexus™ device; the intervention was carried out following a debranching procedure to set up a bypass between the right common carotid (RCC) and LCC, as well as the LCC and LSA. The procedure was successful and restored flow in the arch whilst successfully excluding the aneurysm, with a suitable proximal sealing length of 3.5 cm from the IA, greater than the minimum recommended length of 3.0 cm. The measured landing diameter of the ascending aorta was 38 mm, and that of the device was 43 mm, thereby producing an oversize ratio of 13.2%. The aneurysmal sac was successfully sealed, both LCC-RCC bypass and LCC-LSA bypass were patent. However, follow-up scans indicated the LCC-RCC bypass remained patent whilst the LCC-LSA bypass was compromised with a thrombus in the bypass near the LCC vascular stroma. A final follow-up of the patient 10 months after the intervention revealed the formation of an aneurysmal sac in the ascending aorta with migration of the ascending module of the device and a suspected leak or tear in the ascending aorta.

The patient had other comorbidities which needed to be taken into consideration during the treatment planning stages. Prior to intervention, the patient was on alendronate 10 mg OD, atorvastatin 20 mg OD, folic acid 5 mg BD, methotrexate 20 mg weekly, omeprazole 20 mg OD, prednisolone 5 mg BD. Following the intervention, the medication was adjusted to alendronate 70 mg OD, aspirin 75 mg OD (for 3 months), atorvastatin 20 mg OD, bisoprolol 1.25 mg OD, clopidogrel 75 mg OD (for 3 months), folic acid 10 mg weekly, methotrexate 15 mg weekly, omeprazole 20 mg OD, prednisolone 10 mg OD.

2.2. Geometric models

Anatomically accurate 3D geometries were reconstructed based on CT scans acquired using an ECG-gated spiral CT scanner

FIGURE 2
The various stages of treatment and follow-ups for the patient examined. PRE: Pre-TEVAR geometry indicating presence of aneurysm, POST: Post-TEVAR geometry following a successfully completed procedure, FU1: First follow-up scan which indicated negative results in the form of the carotid–carotid bypass being compromised, FU2: The final clinical images obtained from the patient indicating the formation of an aneurysmal sac in the ascending aorta.
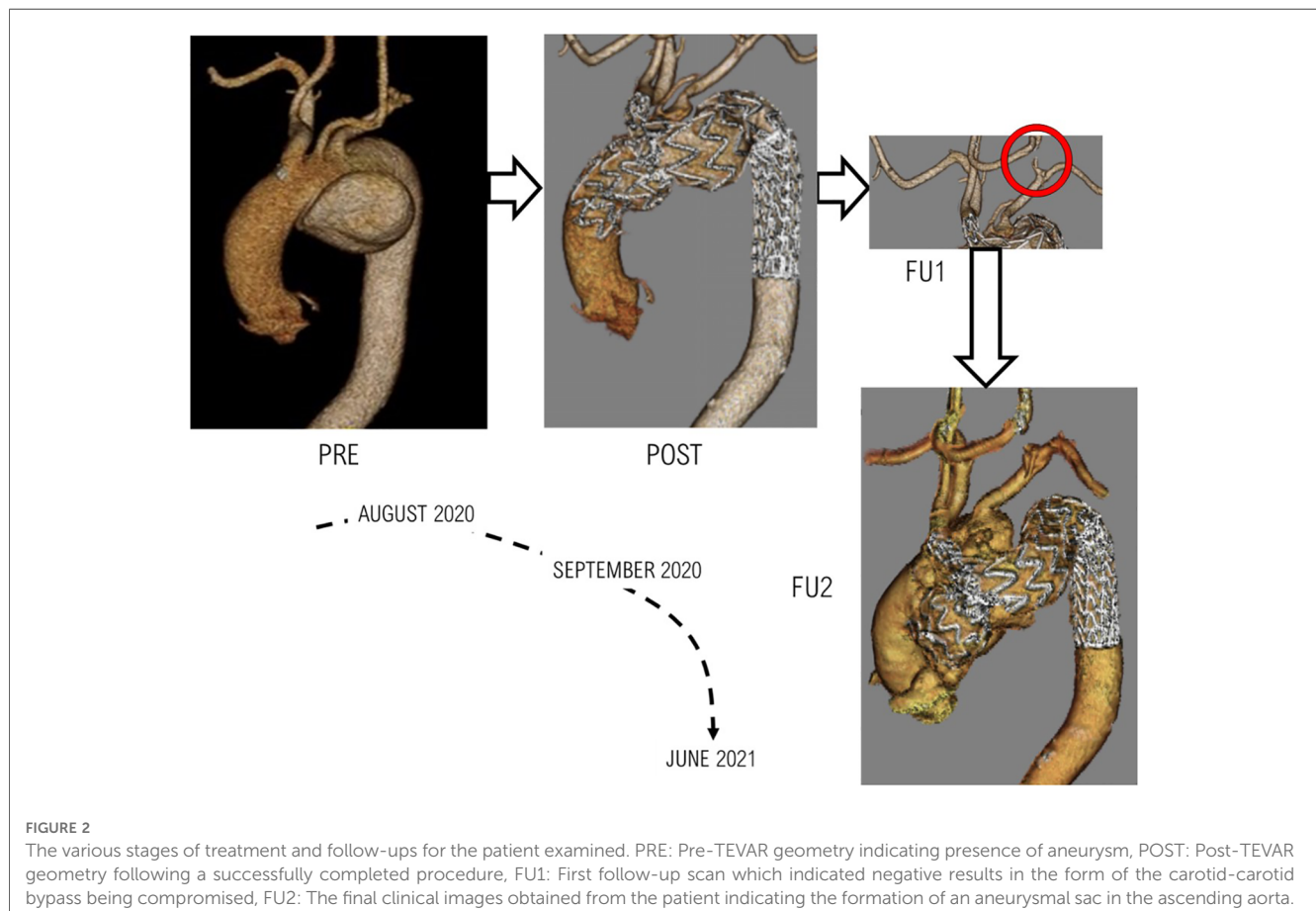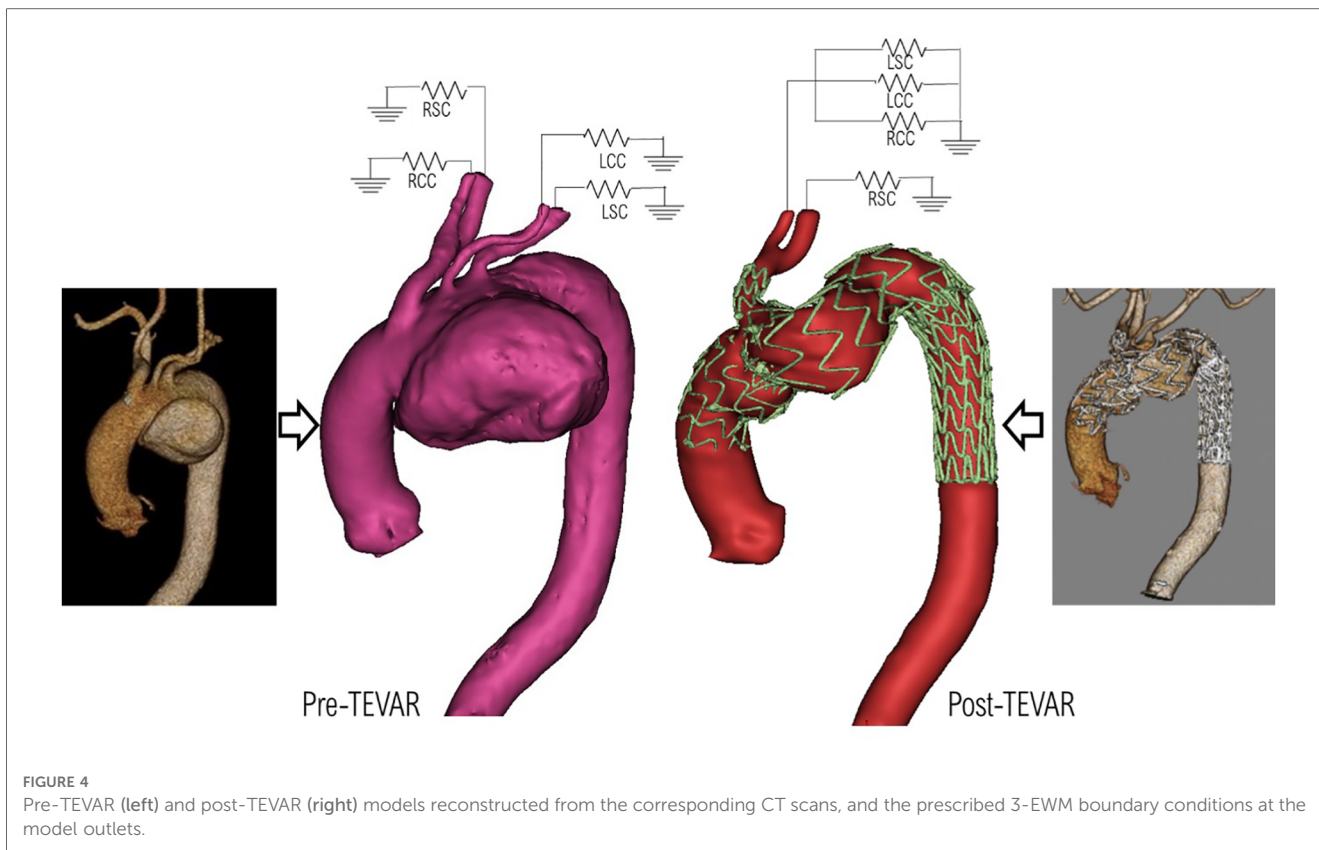
FIGURE 3
Central line view of the whole aorta: (left) proximal to distal aorta with three marked levels. (A)—just beyond LSA, (B)—just before IA, (C)—proximal landing zone, 35 mm from IA proximally to the ascending aorta. The length between (B) and (C) is 35 mm, and (B) and (A) is 70.7 mm. (Right) Transverse view of levels (B) and (C) with a cross-sectional measurement of aortic diameter 37.9 × 37.7 mm and 37.0 × 39.5 mm, respectively.

(Siemens Somatom) at various stages as described in **Figure 2**. Image segmentation and 3D reconstruction of the aorta were performed using an image processing software, Mimics (v20, Materialise, Leuven, Belgium). A thresholding technique was adopted to isolate the regions of interest (ROI). User-defined lower and upper limits of grayscale intensity were set for thresholding, with a typical lower limit of 270–280 HU and an upper limit of 2,000 HU or above depending on the image resolution. This produced initial 2D masks on all the available slices. A split mask function was then used to separate the ROI from unwanted neighboring tissues that might have been included in the initial masks. The separated masks were manually inspected and modified if necessary to ensure all pixels in the targeted vessels were selected. Finally, the reconstructed geometries were smoothed using the Discrete Gaussian filter based on a linear smoothing enhancement algorithm. The smoothing function requires a smoothing factor (within range 0–1) and the number of iterations (within range 1–500) to be specified. A specific "compensate shrinkage" feature was enabled to preserve the shape of the geometry, thereby preventing the lumen of the aorta and its branches from shrinking. This was ensured by comparing vessel diameters extracted from the reconstructed 3D surface with those measured in the CT images at multiple locations of interest. Sensitivity tests indicated that setting a smoothing

factor of 0.1 and 50 iterations for each stage of smoothing produced reliable reconstructions used in this study. **Figure 4** shows the pre-TEVAR geometry which featured a large aortic arch aneurysm in the inferior radius of the arch and three supra-aortic branches emerging from the arch. The model also included the right brachiocephalic artery and RCC which bifurcate from the IA, resulting in four model outlets in the arch. The post-TEVAR geometry (**Figure 3**) incorporated the implanted device where the two modules were considered as one body and connected with the unstented portions of the aorta. The IA branch and its bifurcation were included while the LCC and LSA were excluded as they were covered by the main module. As a result, the post-TEVAR geometry had two outlets in the arch.

Mesh generation was carried out using ANSYS ICEM CFD (v15.0, ANSYS Inc., Canonsburg, PA, USA). For haemodynamic analysis, unstructured meshes consisting of 10 prismatic boundary layers at the wall were generated with approximately 6.8 and 5 million elements in the post-TEVAR and pre-TEVAR geometries respectively. For biomechanical structural analysis, a constant wall thickness of 1.4 mm was applied to the reconstructed 3D luminal surface, creating a solid volume representing the aortic wall. **Figure 5** shows the solid domain geometry consisting of 6.8 million elements and the delineation of the stented and unstented regions.

FIGURE 4
Pre-TEVAR (left) and post-TEVAR (right) models reconstructed from the corresponding CT scans, and the prescribed 3-EWM boundary conditions at the model outlets.

2.3. Computational details and boundary conditions

Flow in the aorta was described by the transient, three-dimensional equations for conservation of mass and momentum. Blood was modelled as a Newtonian fluid with a constant density

FIGURE 5
3d geometry for structural domain, with unstructured mesh shown on the left, and segments of different material highlighted on the right. The uniform thickness of the geometry can be seen clearly on the right with the branch inlets and outlets serving as regions of fixed points to tether the geometry in place.

of 1,060 kgm^{-3} and dynamic viscosity of 0.004 Pa s. Based on the measured peak flowrate of $2.34 \times 10^{-4}\,m^3/s$ and inlet area of 993.13 mm^2, the peak Reynolds number was 2,182.3 and the corresponding Womersley number was 19.2. This combination indicated that flow in the ascending aorta was likely to be disturbed [20], hence the need to employ the SST-Tran (shear stress transport—transitional) model, which has been shown to be more suitable for physiological flows involving potential transition from laminar to turbulent flow [21, 22].
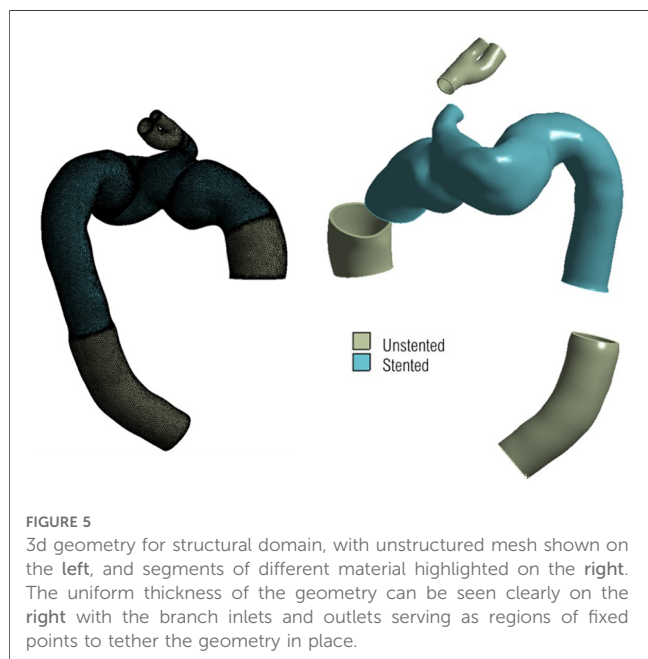
In order to solve the flow governing equations numerically, suitable boundary conditions at the inlet and outlets are required. These should, as much as possible, represent the flow conditions specific to the patient and the stage of treatment being considered. The inflow waveform was adapted from a previous study [22] and then adjusted to represent the recorded cardiac output of the patient and further tuned to the dimensions of the model inlet [23, 24]. The lack of patient-specific inflow data, such as 4D Flow MRI specific to the patient, necessitated the implementation of a novel method for generating realistic 3D inlet velocity profiles (IVPs). A synthetic dataset of virtual aortic velocity profiles was generated by employing statistical shape modelling (SSM) to a clinical dataset consisting of 31 thoracic aortic aneurysm (TAA) cases; this produced representative 3D IVPs comparable to that of the velocity distributions observed whilst using specific 4D Flow MRI data [25]. The velocity profile producing peak systolic velocity closest to that of the clinical measurement was chosen and interpolated in time to match the length of the cardiac cycle. Figure 6 shows the generated IVPs
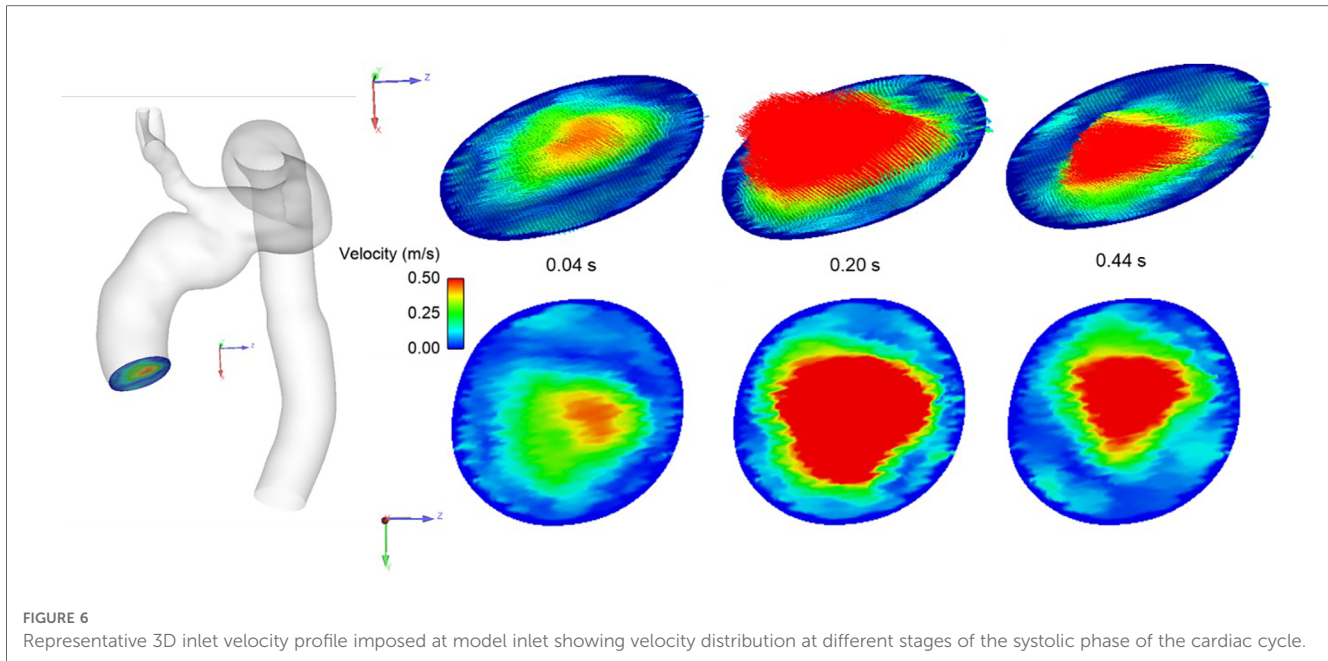
FIGURE 6
Representative 3D inlet velocity profile imposed at model inlet showing velocity distribution at different stages of the systolic phase of the cardiac cycle.

prescribed at the model inlet. The length of the cycle was adjusted according to the heart rate (HR) of the patient (Pre-TEVAR HR: 74 beats/minute, Post-TEVAR HR: 84 beats/min).

A 3-element Windkessel model (3-EWM) was prescribed at the outlets and tuned according to blood pressure measurements made throughout the observation and treatment phases (pre-TEVAR aortic pressure: 119/72 mmHg, post-TEVAR brachial pressure: 133/62 mmHg) using an established method (26). Since the 3-EWM requires mean arterial pressure (MAP) values for the necessary parameters to be set, MAP was calculated from the measured systolic and diastolic pressures (SP and DP respectively) (27).

$$MAP = DP + \frac{1}{3}(SP - DP)$$

Since the measured post-TEVAR pressure corresponded to the brachial (*brach*) pressure, which cannot be directly utilised for the 3-EWM, the measured brachial pressure was converted to central (*cent*) pressure using the following expression (28), with $DP_{cent} = DP_{brach}$,

$$SP_{brach} \approx 0.83 SP_{cent} + 0.15 DP_{cent}$$

All the model parameters used in the 3-EWM are given in **Table 1**. In addition, the employment of SST-Tran model required a turbulence intensity (Tu) to be prescribed at the inlet. A low Tu of 1% was set based on previous experience (21, 22). The wall was assumed to be rigid with a no-slip boundary condition. CFD simulations were carried out using ANSYS CFX v15.0 (ANSYS, Canonsburg, PA, United States) with a fixed time-step of 0.001 s and a convergence criterion of 10^{-5}. All simulations were run for at least 3 cycles until a periodic solution was reached.

TABLE 1 3-EWM parameters used in the three models simulated in this study.

Model	Outlet	R1 [Pa s m^{-3}] ($\times 10^7$)	C [m^3 Pa^{-1}] ($\times 10^{-9}$)	R2 [Pa s m^{-3}] ($\times 10^8$)
PRE	RSA	5.75	1.07	16.2
	RCCA	9.94	0.669	25.8
	LCCA	24.4	0.399	42.4
	LSA	9.63	0.868	19.7
	OUT	1.20	6.98	2.45
POST	RSA	5.75	1.03	16.8
	RCCA	4.02	1.03	9.19
	OUT	1.20	5.13	2.54
FU1	RSA	5.75	1.03	1.68
	RCCA	6.91	1.03	16.7
	OUT	1.20	7.56	2.25

RSA, Right subclavian artery; RCCA, Right common carotid artery; LCCA, Left common carotid artery; LSA, Left subclavian artery; OUT, model outlet).

For finite element analysis (FEA) of wall deformation and stress in the post-TEVAR model, the native aorta was assumed to be an isotropic, homogeneous and linear elastic material with a Young's modulus (E) of 0.8 MPa and Poisson's ratio (*v*) of 0.49 (29). The stented region was also modelled as a linear elastic material with a Young's modulus of 15 MPa and Poisson's ratio of 0.3 (30, 31). The material densities were 1,100 kg.m^{-3} and 2,140 kg.m^{-3} for the native aorta and stented region respectively (30) (Molony et al., 2009). Since the aortic wall model was reconstructed from CT images obtained at diastole, it was necessary to account for prestress in the aorta under diastolic pressure conditions. Prestress was estimated using an iterative approach proposed and evaluated in previous studies (32, 33). The iterative process was carried out until the maximum total deformation in the stressed configuration was less than 0.5 mm under a diastolic pressure, allowing for the structural domain to

TABLE 2 Haemodynamic indices used for analysis in this study.

Metric	Mathematical expression	Description
Time-averaged WSS	$TAWSS = \frac{1}{T}\int_0^T \lvert\tau_w\rvert dt$	Average of the WSS magnitude over the cardiac cycle.
Transverse WSS	$TransWSS = \frac{1}{T}\int_0^T \left\lvert \tau_w \cdot \left(n \times \frac{\int_0^T \tau_w dt}{\lvert\int_0^T \tau_w dt\rvert} \right) \right\rvert dt$	Average over the cardiac cycle of WSS components perpendicular to the temporal mean WSS vector.
λ_2 criterion	$\lambda_2 = \frac{\partial v_x}{\partial y}\frac{\partial v_y}{\partial x} + \left(\frac{\partial v_y}{\partial y}\right)^2 + \frac{\partial v_y}{\partial z}\frac{\partial v_z}{\partial y}$	Synthetic descriptor for incompressible flows used to evaluate isosurfaces in flow.
Displacement force	$F_{d,i} = \int_{A,i} p\,dA + \int_{A,i} \left(-\eta_w \frac{\partial u_t}{\partial n}\right) dA$	Time dependent displacement force due to pressure and friction exerted by the flow of blood on the walls.
Oscillatory shear index	$OSI = \frac{1}{2}\left(1 - \frac{\lvert\int_0^T \tau_w dt\rvert}{\int_0^T \lvert\tau_w\rvert dt}\right)$	Change of direction of the WSS vector from the primary direction of flow.
Endothelial cell activation potential	$ECAP = \frac{OSI}{TAWSS}$	Synthetic metric to identify regions at a higher risk of thrombus formation.

T is the time period of a cardiac cycle; τ_w is the wall shear stress vector; v_x, v_y, v_z are the velocity components in the x, y, and z direction; u_t is the tangential velocity with respect to the unit normal for each element.

achieve equilibrium with the internal blood pressure (34). The obtained prestress tensor was then applied in the FEA simulation where the geometry was tethered at the inlet and branch outlets and peak systolic pressure distribution from the flow simulations were applied as the load at the internal surface of the wall model. All FEA simulations were carried out using ANSYS Static Structural v19.2 (ANSYS, Canonsburg, PA, United States).

2.4. Haemodynamic metrics and endograft dynamics

This investigation explores the haemodynamic response to the implanted device, focusing on localised flow patterns, WSS-related metrics and flow disturbances. A list of the indices used here are defined in **Table 2**. A detailed description of the relevant haemodynamic metrics for the investigation can be found in our previous work (14).

3. Results

3.1. Flow patterns

Figure 7 shows instantaneous streamlines at peak systole for all the simulated scenarios (PRE, POST, and FU1). Flow in the ascending aorta was helical with high velocities skewed towards the outer curvature in all models. The presence of the aneurysm in the arch (PRE) caused a large recirculation zone in the aneurysm sac. Excluding the aneurysm *via* TEVAR restored a more desirable flow pattern in the arch, as can be seen in POST. This not only led to more uniform flow into the supra-aortic branches, but also virtually eliminated any undesirable recirculating flow in the arch. Aside from small differences in the supra-aortic branches, there seem to be no qualitative differences in flow patterns between POST and FU1.

Comparison of the time-varying outflow through the RCC outlet is given in **Figure 8** for the three simulated scenarios. The large recirculation zone in the aneurysm sac affected perfusion of
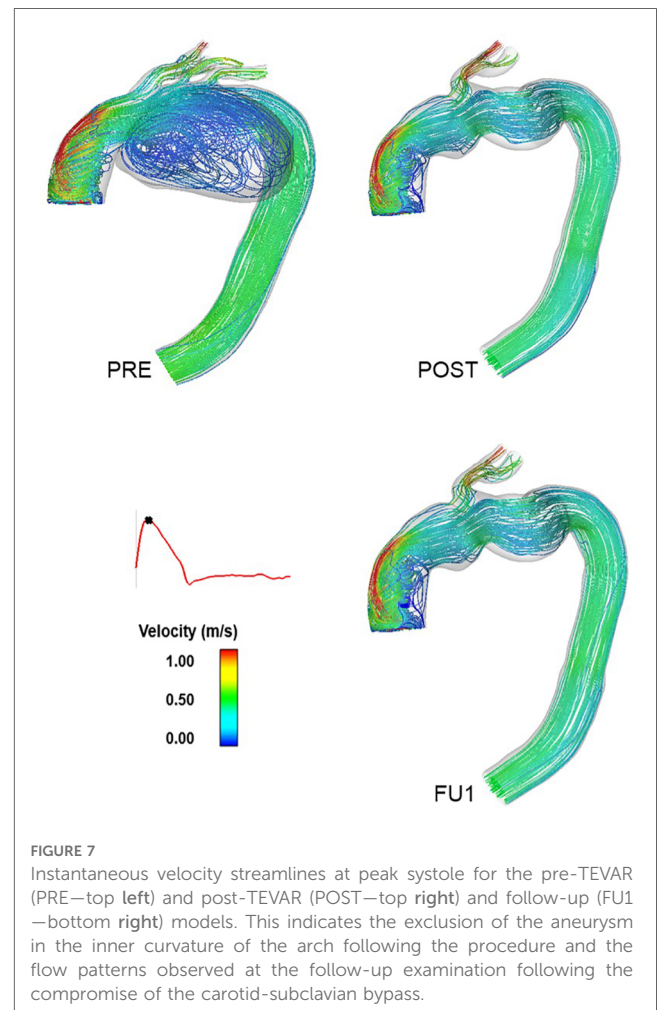
the arch branches in PRE where flow through the RCC outlet was retrograde for approximately 64% of the cardiac cycle. PRE also had a lower peak flowrate and significantly lower flow throughout the cycle, providing a mean outflow of 3.48×10^{-6} m^{3}s^{-1} (0.21 L/min) through the RCC. Other arch branches also experienced large periods of retrograde flow ranging between

FIGURE 7
Instantaneous velocity streamlines at peak systole for the pre-TEVAR (PRE—top **left**) and post-TEVAR (POST—top **right**) and follow-up (FU1 —bottom **right**) models. This indicates the exclusion of the aneurysm in the inner curvature of the arch following the procedure and the flow patterns observed at the follow-up examination following the compromise of the carotid-subclavian bypass.
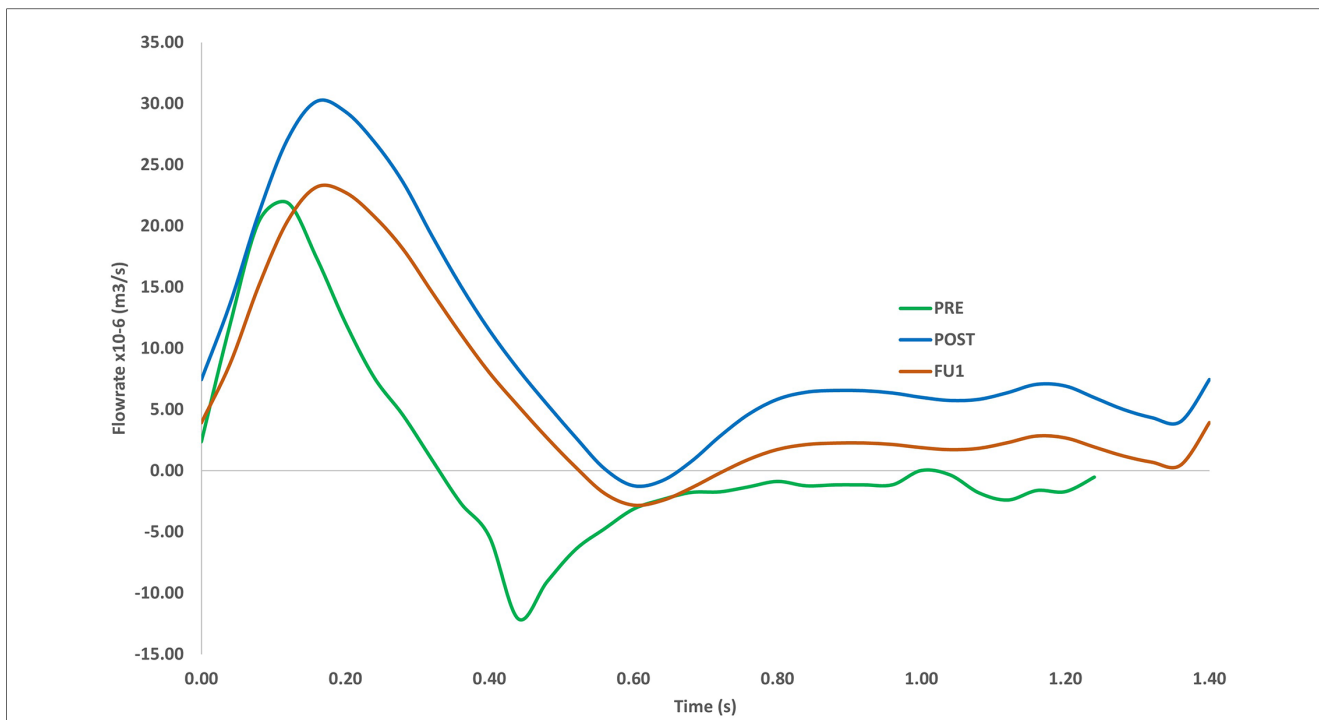
FIGURE 8
Volumetric flowrate in the RCC for the pre-TEVAR (PRE) case, post-TEVAR (POST) and follow-up (FU1) cases **(bottom)**. The length of the cardiac cycle was based on clinical measurements (1.23 s for pre-TEVAR and 1.4 s for post-TEVAR).

64%–69% of the cardiac cycle. Post-TEVAR flow through the RCC was mostly antegrade with a mean outflow of $9.59 \times 10^{-6}\,\mathrm{m^3 s^{-1}}$ (0.57 L/min). The difference in outflow between POST and FU1 was due to the altered boundary conditions in FU1 to represent the break in the carotid-subclavian bypass further downstream of

the RCC. As a result, FU1 had a lower flow rate of $5.55 \times 10^{-6}\,\mathrm{m^3 s^{-1}}$ (0.33 L/min) through the RCC.

The vortical flow structure throughout the modelled aorta is visualised using the λ_2 criterion as shown in **Figure 9**. A threshold value of $-100\ \mathrm{s^{-2}}$ was chosen in order to isolate the

PRE λ_2-criterion threshold: $-100\ \mathrm{s^{-2}}$ POST
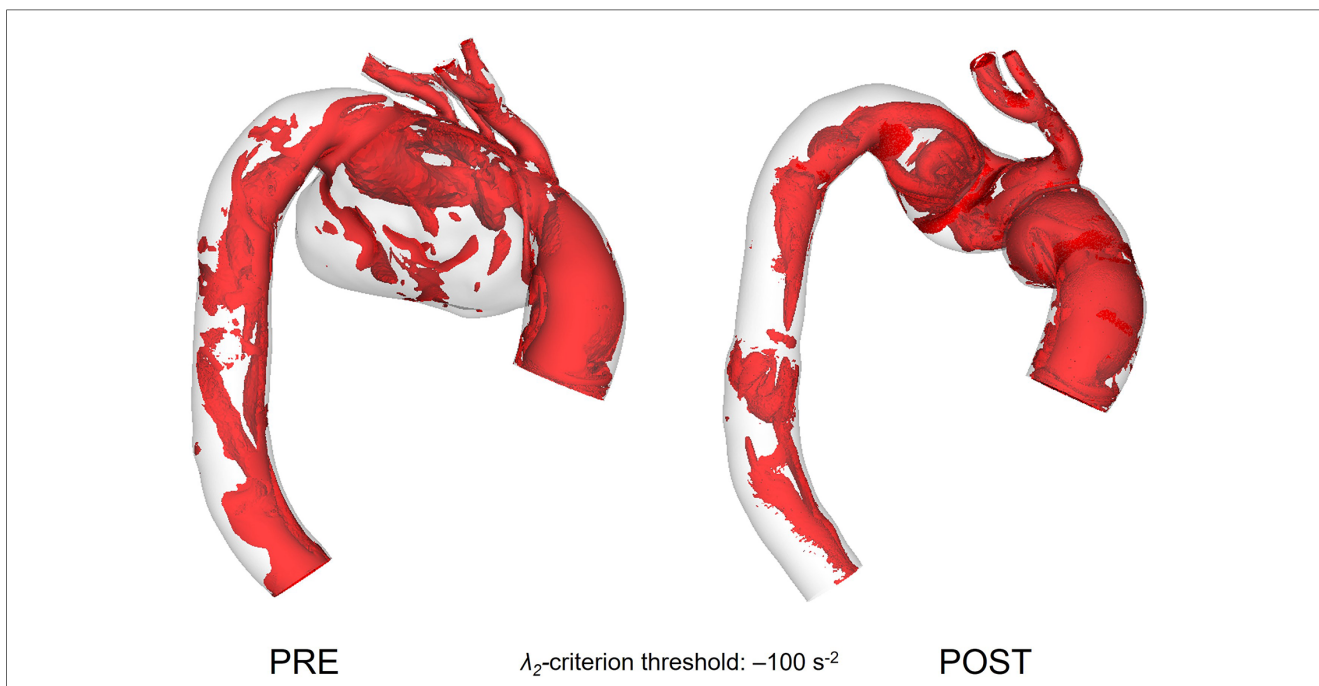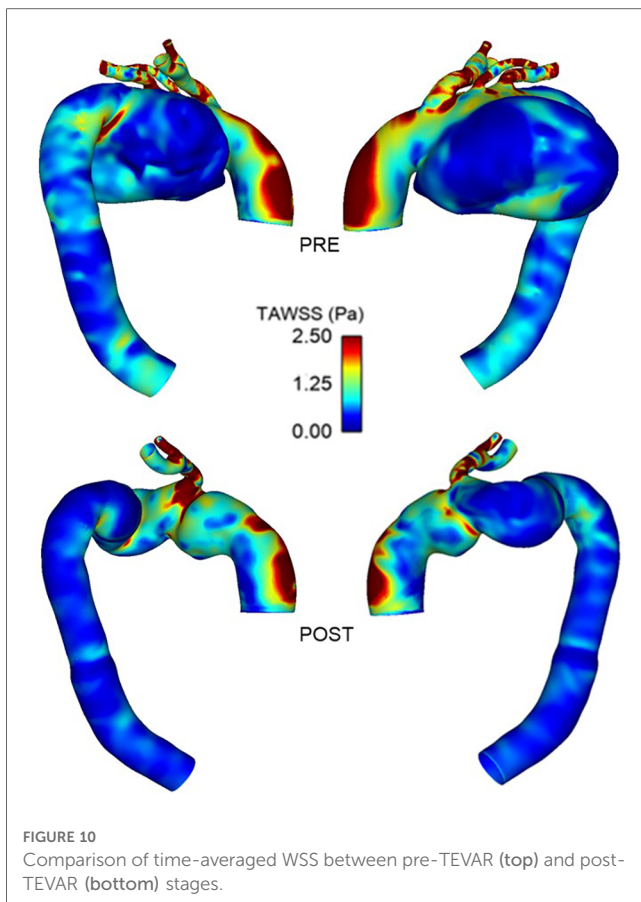
FIGURE 9
Vortical structures within the vessel represented as isosurfaces using the λ_2 criterion for pre-TEVAR **(left)** and post-TEVAR **(right)** stages.

FIGURE 10
Comparison of time-averaged WSS between pre-TEVAR (**top**) and post-TEVAR (**bottom**) stages.

FIGURE 11
Comparison of wall shear stress-related metrics between post-TEVAR and follow-up stages with time-averaged WSS (**top**), transverse WSS (**middle**) and endothelial cell activation potential (**bottom**) maps all showing similar spatial distribution and patterns between the two cases.

relevant vortex cores formed in the aorta and to make suitable qualitative comparisons. Pre-TEVAR aneurysmatic flow understandably presented with a greater degree of disturbance as flow entered the arch branches compared to the post-TEVAR model which presented with vortical flow that can be often seen in and attributed to the curved nature of the vessel giving rise to counter-rotating vortices.

3.2. Wall shear stress related indices

Wall shear stress and its associated indices are important near wall haemodynamic parameters which can affect endothelial cell proliferation and play a role in thrombus formation (35, 36). **Figure 10** demonstrates the difference in time-averaged WSS (TAWSS) patterns between PRE and POST. Both present with a large area of high TAWSS along the outer curvature of the ascending aorta, which is due to the skewed inlet velocity profile and the curvature of the aorta. The large recirculation zone in the aneurysmal sac, as seen in **Figure 7**, led to extremely low TAWSS in this area (PRE), with elevated TAWSS along the outer curvature of the arch and in the emerging branches. In the PRE model, a patch of elevated (>2.5 Pa) TAWSS can be seen in the inner curvature of the arch, immediately downstream of the aneurysm.

Comparisons of WSS-related indices between POST and FU1 are shown in **Figure 11**, displaying high degree of similarities. TAWSS and transverse WSS (transWSS) are useful metrics which serve as
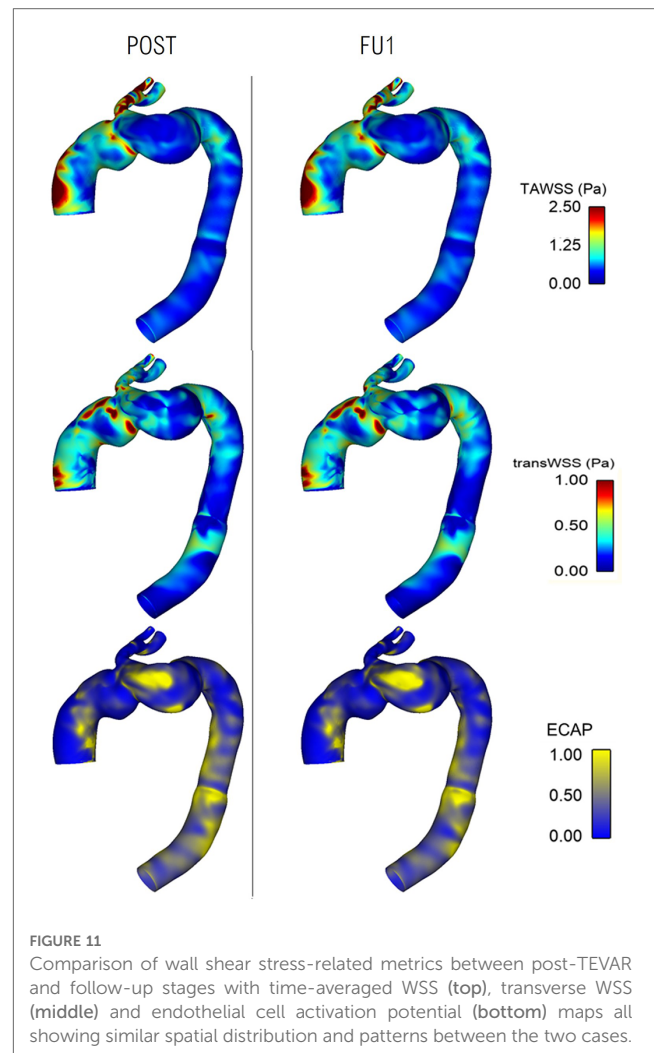
indicators for thrombus formation and plaque development, and there appears to be no extremes of magnitudes or abnormal spatial distribution of either. Endothelial cell activation potential (ECAP) identifies regions of high oscillatory shear index (OSI) and low TAWSS and regions of ECAP higher than 5.0 can pose a risk of thrombus formation (37, 38). However, in these cases there appears to be no abnormally high values of ECAP.

3.3. Displacement force

The implanted SG experiences a displacement force (DF) resulting from the change in net momentum owing to pressure and WSS generated by the aortic blood flow. Since pressure is the dominant component, the time-varying nature of displacement force is expected to closely resemble the pressure waveform (39). **Figure 12** shows the displacement force acting on the ascending module of the endograft in POST, decomposed into three orthogonal components as defined in the figure. The displacement force was primarily in the z-direction but with a significant component in the y-direction due to the non-planar curvature of the aorta, thus along the coronal plane for the individual.
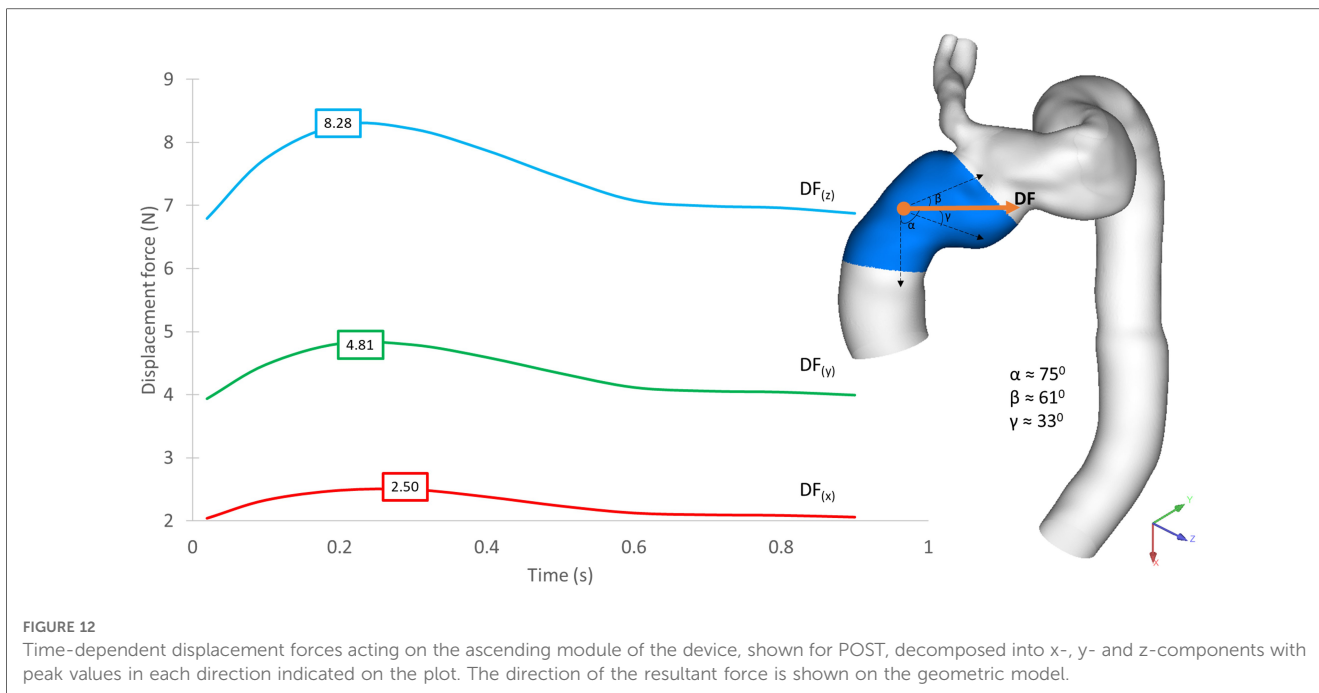
FIGURE 12
Time-dependent displacement forces acting on the ascending module of the device, shown for POST, decomposed into x-, y- and z-components with peak values in each direction indicated on the plot. The direction of the resultant force is shown on the geometric model.

Figure 13 demonstrates the difference in displacement force between POST and FU1, with the endograft experiencing a consistently higher force in FU1 than in POST throughout the cycle. The maximum displacement force in FU1 was 15% higher than in POST.

Since the ascending module of the device is of particular interest in this case, it was further divided into separate segments, and the magnitude of displacement force was calculated for each of these segments. As shown in **Figure 14**, the distribution of displacement force was non-uniform with
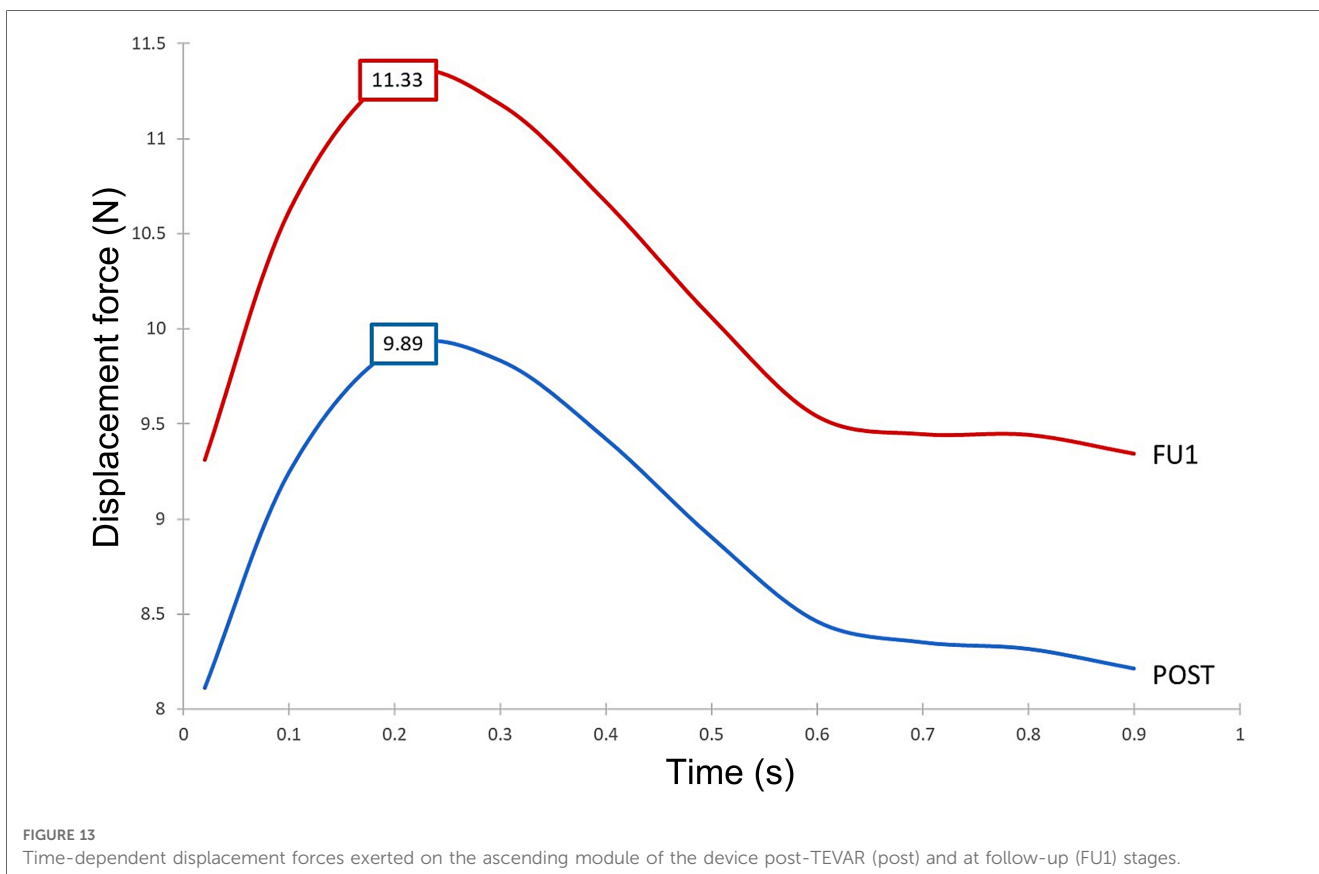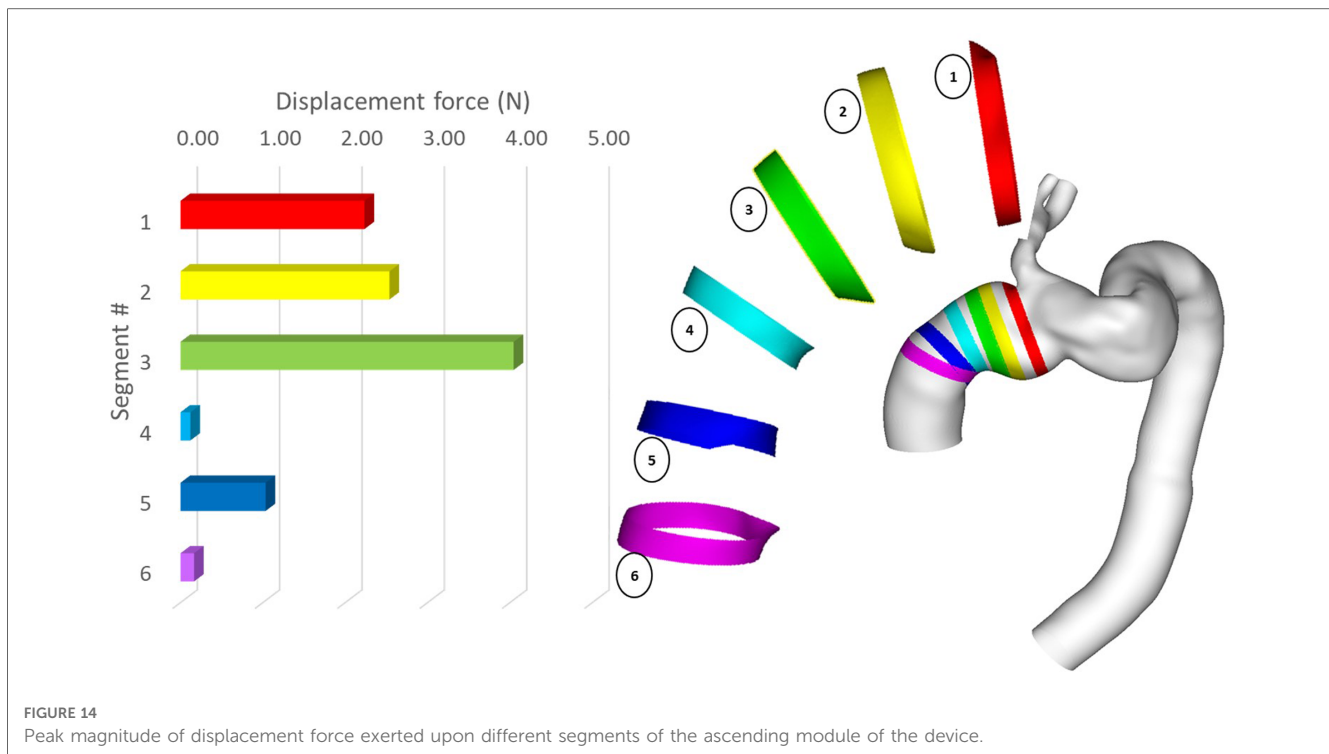

FIGURE 13
Time-dependent displacement forces exerted on the ascending module of the device post-TEVAR (post) and at follow-up (FU1) stages.

FIGURE 14
Peak magnitude of displacement force exerted upon different segments of the ascending module of the device.
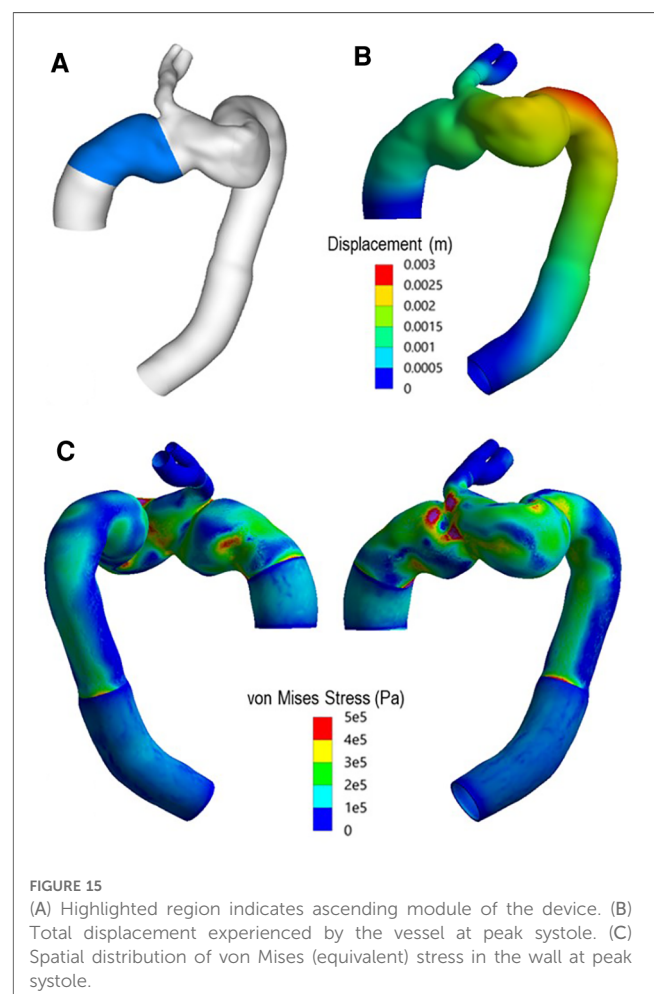
larger values in the distal portion of the ascending module. Segment 3 experienced the largest displacement force, followed by segment 2 and 1, which are closer to the overlapping region between the ascending module and the main endograft.

3.4. Wall displacement and mechanical stress

Figure 15 presents the spatial distribution of wall displacement and von Mises stress (equivalent stress) obtained with the FE analysis. The structural analysis was carried out at peak systole to represent the worst-case scenario when the aorta was subjected to the maximum pressure load. The highest von Mises stresses were observed in the distal ascending aorta, immediately upstream of the emerging branch. This coincides with the previously highlighted overlapping region between the two modules. The maximum displacement of up to 2.41 mm was observed at the distal end of the arch and could be attributed to the region not being anchored by the LCC and LSA.

4. Discussion

The case analysed in this investigation presented with a rather complex pathology along with several comorbidities that had to be taken into account when determining treatment for the patient. TEVAR was considered the best option due to its minimally invasive nature and the availability of the device to exclude the aneurysm and restore flow in the region. The chosen device was a single-branched aortic arch endograft with a side branch

FIGURE 15
(A) Highlighted region indicates ascending module of the device. (B) Total displacement experienced by the vessel at peak systole. (C) Spatial distribution of von Mises (equivalent) stress in the wall at peak systole.

leading into the innominate artery. Revascularisation was carried out prior to the TEVAR procedure by introducing bypasses from the RCC to LCC and LCC to LSA. Clinical information and the second follow-up CT examination (as shown in **Figure 2** at FU2) indicated the formation of a new aneurysm in the ascending aorta, with migration of the ascending module of the device and a suspected leak or tear in the ascending aorta.

4.1. Comparing pre- and post-intervention haemodynamics

As shown in **Figure 7**, the presence of a large aneurysm in the arch caused a significant reduction in flow velocity and recirculating flow in this region, which adversely influenced the flow leading into the arch vessels as reported by others (13). This was evidenced through a prolonged period of retrograde flow through the RCC (**Figure 8**), which could impair blood perfusion further downstream. Multidirectional flow can also lead to extreme WSS, which may increase the risk for thrombus formation and/or atherosclerotic lesion development in the supra-aortic arteries (40).

The TEVAR procedure using a single branched endograft successfully excluded the aneurysm and restored more organised flow in the arch. A smoother lumen, in the absence of the aneurysm, allowed for sufficient flow leading into the IA, which in turn perfused the LCC and LSA through the bypass performed pre-TEVAR. Nevertheless, the non-planar and tortuous geometry of the arch was exacerbated after the endograft was deployed as can be seen from the post-TEVAR geometry (**Figure 4**). The procedure also resulted in increased flow into the IA, which was the only supra-aortic branch directly perfused through the arch and it had to carry additional flow to supply the LCC and LSA. The choice of device was made based on the complex nature of the region being treated and to ensure sufficient perfusion to the supra-aortic branches. Branched and fenestrated endografts would both serve the purpose of aortic branch perfusion, but the local haemodynamics will be influenced by the endograft design. Using a branched stent-graft allows for flow to be smoothly guided into the emerging arch branch. Additionally, the ability of the main module of the single branched device to be securely anchored in the deployed region made it the more suitable choice in this case.

4.2. Post-intervention and beyond

Flow patterns in the POST and FU1 were largely similar throughout the aorta, with a small difference in the IA due to the different outflow through the RCC branch. Close examination of WSS-related indices also revealed no significant alteration between POST and FU1 as shown in **Figure 11**, suggesting that the minor change in outflow conditions through the RCC in FU1 had not affected the global flow patterns and near wall haemodynamics.

It was clear from the final follow-up (FU2) CT scan (**Figure 2**) that further complications occurred between FU1 and FU2. The scan revealed the formation of a large aneurysm alongside the

ascending module of the device, which extended along the outer curvature of the arch. Flow through this bulge perfused the native ostia of the LSA and LCC which were initially occluded prior to the TEVAR procedure. It was suspected that a leak or tear occurred in the ascending aorta, but the origin of the leak was undetermined, and a suspected source of the leak could be migration of the device or dehiscence due to improper fixation. This necessitated a closer examination of the biomechanical environment of the ascending aorta in searching for a plausible cause for the suspected leak.

Firstly, the possibility of device migration was assessed. The main module of the device was unlikely to move as it was anchored securely by the branch leading into the IA, but the ascending module was connected to the main module through a self-protecting sleeve and relied on a radial force interlocking mechanism to hold it in place. Migration of the ascending module could occur if the displacement force (DF) acting on it was sufficient to move it upward or pull it away from the main module, which would lead to type I or type III endoleak respectively (41). Previous studies suggested that DF exerted on the endograft can have a considerable effect on its spatial stability (42), and that the magnitude and direction of DF are influenced by the endograft geometry, the haemodynamic state of the patient, and the local geometry of the vessel (39, 43–45). Therefore, it was necessary to evaluate the DF experienced by the ascending module in both POST and FU1.

Our results showed that despite overall flow patterns being largely similar between POST and FU1, the DF increased by approximately 15% in FU1. The only difference between the POST and FU1 models was the outflow conditions imposed at the outlets. As has already been mentioned, the boundary conditions were altered to reflect the compromised LCC-LSA bypass, with excess flow being diverted to the descending aorta. This redirected flow resulted in changes in the normal pressure forces on the vessel wall, leading to an increase in DF. Nevertheless, the maximum DF of 11.33 N in FU1 was well below the reported threshold of 32 N to dislocate a non-planar stent-graft in the thoracic aorta (46). While threshold values have been reported for the abdominal and thoracic aorta (47, 48), there is little information in the literature on the magnitude of DF needed to cause device migration in the ascending aorta. It was also interesting to note the direction of DF as illustrated in **Figure 12** which shows clearly that the total DF experienced by the ascending module deviates from its local longitudinal direction. This was attributed to the curvature and non-planarity of the aorta, especially in the region of interest here, giving rise to increased anterio-posterior and lateral components (43). The direction of DF vector indicated that it would pull the ascending module laterally away from the outer curvature, which could compromise the stability in the proximal landing zone or lead to misalignment in the device (18, 19). Further analysis of the distribution of DF along the ascending module showed that the region close to the connection between the two modules experienced relatively high DF (**Figure 14**).

The spatial distribution of von Mises stress obtained with the finite element analysis showed high stresses in the region where the

two parts of the device connect (**Figure 15**), owing to the highly tortuous local geometry and the emergence of the IA branch. The maximum von Mises stress was approximately 1.3 MPa, which exceeded the yield stress for dilated ascending aorta of 1.2 ± 0.1 MPa referenced in other studies (49, 50). Although the maximum stress occurred in the wall protected by the endograft, and the graft is much stiffer and can withstand higher stresses compared to the native aorta, the extremely high level of stress in this region could compromise the device locking mechanism, thereby increasing the risk of disconnection between the two modules. Moreover, high stress concentrations were also observed in the proximal and distal ends of the device, resulting from local geometric discontinuity and compliance mismatch between the graft and the native aorta. Such focal high stress regions have been found to correlate strongly with the locations of stent-graft induced new entry in type B aortic dissections (51, 52). Based on these findings, it is plausible to speculate that a proximal tear might have occurred which then led to the formation of the observed aneurysm.

4.3. Limitations

In the CFD simulations presented in this investigation, the aortic wall was assumed to be rigid and the supra-aortic vessels bypass was not included in the post-TEVAR model. The rigid wall assumption is expected to have a minor influence on the predicted flow patterns, especially in the post-TEVAR and follow-up models where a large part of the aorta was supported by the endograft. Excluding the supra-aortic vessels bypass is also likely to have an insignificant effect on the predicted haemodynamics and wall stress, even though its inclusion would have provided the opportunity to investigate potential causes for the failed carotid-subclavian bypass observed at FU1. In the finite element stress analysis, the aortic wall was modelled as a linear elastic material; this assumption was made because within the region of interest, the post-TEVAR aortic wall was largely integrated with the endograft with a relatively small section of the native aorta at the proximal and distal end of the device. In addition, the periodic motion of the aortic root and its influence on the ascending aorta were ignore, which could have influenced the predicted wall stress (53). Finally, the results presented here were confined to a single patient. However, the number of patients undergoing TEVAR of the entire aortic arch with a single-branched device is very limited and this paper focused on presenting a longitudinal analysis at multiple stages of the treatment.

5. Conclusion

This investigation presents a detailed haemodynamic and biomechanical analysis of a patient who underwent TEVAR treatment for a large aneurysm in the aortic arch using a single-branched endograft. Imaging data from different stages of the process along with physiologically representative numerical modelling allowed to paint a picture of the progression of the case from pre-intervention to post-intervention and beyond. Simulation results for the different stages demonstrated the dramatic improvement in flow

patterns in the aortic arch after the TEVAR procedure. As the final follow-up examination revealed the formation of a new aneurysm in the ascending aorta, further analysis was carried out in searching for possible causes for the observed complication. Results for displacement forces on the endograft and stresses within the wall indicated that the endograft was subjected to an angulated displacement force in the lateral direction and the overlapping region between the main and ascending module experienced very high stresses, which could act together to weaken the locking system, resulting in migration or misalignment of the device. In addition, high stress concentration was observed at the proximal end of the ascending module, suggesting the possibility of a proximal tear as a source for the observed aneurysm. Careful positioning of the overlapping region and the proximal landing zone may help reduce the stresses in these regions at risk of compromising stent-graft stability. In this regard, finite element-based simulations of virtual stent-graft deployment, such as those reported recently on aortic dissections (53, 54), offer a promising tool that should be further developed and validated for use in pre-intervention planning to minimise potential device migration or endoleaks.

Data availability statement

The raw data supporting the conclusions of this article will be made available by the authors, without undue reservation.

Author contributions

Conceptualisation, XX and CN; methodology, SS; software, SS, LM and SP; validation, SS; formal analysis, SS and XY; investigation, SS; resources, XX; data curation, SS, XY, CN, and SP; writing—original draft preparation, SS; writing—review and editing, XX, SS, XY and CN; visualization, SS and XY; supervision, XX; project administration, XX; funding acquisition, XX. All authors have read and agreed to the published version of the manuscript. All authors contributed to the article and approved the submitted version.

Funding

Acknowledgements

and Mr Simone Saitta, Department of Electronics, Information and Bioengineering, Politecnico di Milano.

Publisher's note

References

1. Crawford ES, Saleh SA, Schuessler JS. Treatment of aneurysm of transverse aortic arch. *J Thorac Cardiovasc Surg*. (1979) 78(3):383–93. doi: 10.1016/S0022-5223(19)38103-6

2. Joseph G. Commentary: treatment of ascending aortic pathology with arch endografts that extend proximally. *J Endovasc Ther*. (2019) 26(4):463–6. SAGE Publications Inc. doi: 10.1177/1526602819856597

3. Natsume K, Shiiya N, Takehara Y, Sugiyama M, Satoh H, Yamashita K, et al. Characterizing saccular aortic arch aneurysms from the geometry-flow dynamics relationship. *J Thorac Cardiovasc Surg*. (2017) 153(6):1413–20. e1. doi: 10.1016/j.jtcvs.2016.11.032

4. Bodell BD, Taylor AC, Patel PJ. Thoracic endovascular aortic repair: review of current devices and treatments options. *Tech Vasc Interv Radiol*. (2018) 21(3):137–45. doi: 10.1053/j.tvir.2018.06.003

5. Han DK, Jokisch C, And B, Mckinsey JF. Expanding the landing zone for TEVAR a discussion of the longevity and durability of commonly used extrathoracic debranching techniques. *Endovascr Today*. (2016) 15(11):85–90.

6. Yuan X, Mitsis A, Mozalbat D, Nienaber CA. Alternative management of proximal aortic dissection: concept and application. *Indian J Thorac Cardiovasc Surg*. (2021) 38(Suppl 1):183–92. Springer. doi: 10.1007/s12055-021-01281-3

7. Martin G, Riga C, Gibbs R, Jenkins M, Hamady M, Bicknell C. Short- and long-term results of hybrid arch and proximal descending thoracic aortic repair: a benchmark for new technologies. *J Endovasc Ther*. (2016) 23(5):783–90. doi: 10.1177/1526602816655446

8. Chiu TL, Tang AYS, Cheng SWK, Chow KW. Analysis of flow patterns on branched endografts for aortic arch aneurysms. *Inform Med Unlocked*. (2018) 13:62–70. doi: 10.1016/j.imu.2018.10.008

9. Haulon S, Kratzberg J, Guihare J, Fabre D. Current Status of arch branch technology. *Endovascular Today*. (2008) 17(11):71–6.

10. Kondov S, Kreibich M, Rylski B, Siepe M, Beyersdorf F, Czerny M. The endovascular repair of the aortic arch using a double branched prosthesis. *J Vis Surg*. (2018) 4:132–132. doi: 10.21037/jovs.2018.05.27

11. Ishimaru S. Endografting of the aortic arch. *J Endovascular Ther*. (2004) 11:62–71. www.jevt.org doi: 10.1177/15266028040110S609

12. Melissano G, Civilini E, Bertoglio L, Calliari F, Setacci F, Calori G, et al. Results of endografting of the aortic arch in different landing zones. *Eur J Vasc Endovasc Surg*. (2007) 33(5):561–6. doi: 10.1016/j.ejvs.2006.11.019

13. Zhu Y, Zhan W, Hamady M, Xu XY. A pilot study of aortic hemodynamics before and after thoracic endovascular repair with a double-branched endograft. *Med Novel Technol Devices*. (2019) 4:100027. doi: 10.1016/j.medntd.2020.100027

14. Sengupta S, Hamady M, Xu XY. Haemodynamic analysis of branched endografts for complex aortic arch repair. *Bioengineering*. (2022) 9(2):45–61. doi: 10.3390/bioengineering9020045

15. van Bakel TM, Arthurs CJ, van Herwaarden JA, Moll FL, Eagle KA, Patel HJ, et al. A computational analysis of different endograft designs for zone 0 aortic arch repair. *Eur J Cardiothorac Surg*. (2018a) 54(2):389–96. doi: 10.1093/ejcts/ezy068

16. Qiao Y, Fan J, Ding Y, Zhu T, Luo K. A primary computational fluid dynamics study of pre-and post-tevar with intentional left subclavian artery coverage in a type b aortic dissection. *J Biomech Eng*. (2019) 141(11):111002-1–7. doi: 10.1115/1.4043881

17. van Bakel TM, de Beaufort HW, Trimarchi S, Marrocco-Trischitta MM, Bismuth J, Moll FL, et al. Status of branched endovascular aortic arch repair. *Ann Cardiothorac Surg*. (2018) 7(3):409–16. doi: 10.21037/acs.2018.03.13

18. D'Onofrio A, Cibin G, Antonello M, Battocchio P, Piazza M, Caraffa R, et al. Endovascular exclusion of the entire aortic arch with branched stent-grafts after surgery for acute type A aortic dissection. *JTCVS Techniques*. (2020) 3:1–8. doi: 10.1016/j.xjtc.2020.04.009

19. Lindsay T, Ouzounian M, Tan K. Early results of arch disease treated with nexus arch endograft. *J Vasc Surg*. (2017) 66(3):e67. doi: 10.1016/j.jvs.2017.07.017

20. Nerem RM, Seed WA. An in vivo study of aortic flow disturbances. *Cardiovasc Res*. (1972) 6:1–14. doi: 10.1093/cvr/6.1.1

21. Kousera CA, Wood NB, Seed WA, Torii R, O'Regan D, Xu XY. A numerical study of aortic flow stability and comparison with in vivo flow measurements. *J Biomech Eng*. (2013) 135(1):01103-1–9. doi: 10.1115/1.4023132

22. Tan FPP, Borghi A, Mohiaddin RH, Wood NB, Thom S, Xu XY. Analysis of flow patterns in a patient-specific thoracic aortic aneurysm model. *Comput Struct*. (2009) 87(11–12):680–90. doi: 10.1016/j.compstruc.2008.09.007

23. Armour C, Guo B, Pirola S, Saitta S, Liu Y, Dong Z, et al. The influence of inlet velocity profile on predicted flow in type B aortic dissection. *Biomech Model Mechanobiol*. (2021) 20:481–90. doi: 10.1007/s10237-020-01395-4

24. Saitta S, Pirola S, Piatti F, Votta E, Lucherini F, Pluchinotta F, et al. Evaluation of 4D flow MRI-based non-invasive pressure assessment in aortic coarctations. *J Biomech*. (2019) 94:13–21. doi: 10.1016/j.jbiomech.2019.07.004

25. Saitta S, Maga L, Armour C, Votta E, O'Regan DP, Salmasi MY, et al. Data-driven generation of 4D velocity profiles in the aneurysmal ascending aorta. *Comput Methods Programs Biomed*. (2022) 233:107468. doi: 10.1016/j.cmpb.2023.107468

26. Pirola S, Cheng Z, Jarral OA, O'Regan DP, Pepper JR, Athanasiou T, et al. On the choice of outlet boundary conditions for patient-specific analysis of aortic flow using computational fluid dynamics. *J Biomech*. (2017) 60:15–21. doi: 10.1016/j.jbiomech.2017.06.005

27. Stokes C, Bonfanti M, Li Z, Xiong J, Chen D, Balabani S, et al. A novel MRI-based data fusion methodology for efficient, personalised, compliant simulations of aortic haemodynamics. *J Biomech*. (2021) 129:110793. doi: 10.1016/j.jbiomech.2021.110793

28. Westerhof N, Stergiopulos N, Noble MIM. Snapshots of hemodynamics. *Snapshots Hemodyn*. (2010). p. 191–246. doi: 10.1007/978-1-4419-6363-5

29. Bäumler K, Vedula V, Sailer AM, Seo J, Chiu P, Mistelbauer G, et al. Fluid–structure interaction simulations of patient-specific aortic dissection. *Biomech Model Mechanobiol*. (2020) 19(5):1607–28. doi: 10.1007/S10237-020-01294-8

30. de Bock S, Iannaccone F, de Beule M, van Loo D, Vermassen F, Verhegghe B, et al. Filling the void: a coalescent numerical and experimental technique to determine aortic stent graft mechanics. *J Biomech*. (2013) 46(14):2477–82. doi: 10.1016/j.jbiomech.2013.07.010

31. Valente R, Mourato A, Brito M, Xavier J, Tomás A, Avril S. Fluid-Structure interaction modeling of ascending thoracic aortic aneurysms in SimVascular. *Biomechanics*. (2022) 2:189–204. doi: 10.3390/BIOMECHANICS2020016

32. Kan X, Ma T, Lin J, Wang L, Dong Z, Xu XY. Patient-specific simulation of stent-graft deployment in type B aortic dissection: model development and validation. *Biomech Model Mechanobiol*. (2021a) 20(6):2247–58. doi: 10.1007/S10237-021-01504-X

33. Votta E, Presicce M, della Corte A, Dellegrottaglie S, Bancone C, Sturla F, et al. A novel approach to the quantification of aortic root in vivo structural mechanics. *Int J Numer Method Biomed Eng*. (2017) 33(9):e2849. doi: 10.1002/cnm.2849

34. Caimi A, Pasquali M, Sturla F, Pluchinotta FR, Giugno L, Carminati M, et al. Prediction of post-stenting biomechanics in coarcted aortas: a pilot finite element study. *J Biomech*. (2020) 105:109796. doi: 10.1016/J.JBIOMECH.2020.109796

35. Mohamied Y, Sherwin SJ, Weinberg PD. Understanding the fluid mechanics behind transverse wall shear stress. *J Biomech*. (2017) 50:102. doi: 10.1016/J.JBIOMECH.2016.11.035

36. Peiffer V, Sherwin SJ, Weinberg PD. Does low and oscillatory wall shear stress correlate spatially with early atherosclerosis? A systematic review. *Cardiovasc Res*. (2013) 99(2):242. doi: 10.1093/CVR/CVT044

37. di Achille P, Tellides G, Figueroa CA, Humphrey JD. A haemodynamic predictor of intraluminal thrombus formation in abdominal aortic aneurysms. *Proc R Soc A*. (2014) 470(2172):20140163. doi: 10.1098/RSPA.2014.0163

38. Kandail HS, Hamady M, Xu XY. Hemodynamic functions of fenestrated stent graft under resting, hypertension, and exercise conditions. *Front Surg.* (2016) 3. doi: 10.3389/fsurg.2016.00035

39. Kandail H, Hamady M, Xu XY. Patient-specific analysis of displacement forces acting on fenestrated stent grafts for endovascular aneurysm repair. *J Biomech.* (2014) 47(14):3546–54. doi: 10.1016/J.JBIOMECH.2014.08.011

40. Andersson M, Lantz J, Ebbers T, Karlsson M. Multidirectional WSS disturbances in stenotic turbulent flows: a pre- and post-intervention study in an aortic coarctation. *J Biomech.* (2017) 51:8–16. doi: 10.1016/j.biomech.2016.11.064

41. Kassem TW. Follow up CT angiography post EVAR: endoleaks detection, classification and management planning. *Egypt J Radiol Nucl Med.* (2017) 48 (3):621–6. doi: 10.1016/J.EJRNM.2017.03.025

42. Tasso P, Lodi Rizzini M, Raptis A, Matsagkas M, de Nisco G, Gallo D, et al. In-stent graft helical flow intensity reduces the risk of migration after endovascular aortic repair. *J Biomech.* (2019) 94:170–9. doi: 10.1016/j.jbiomech.2019.07.034

43. Figueroa CA, Zarins CK. Computational analysis of displacement forces acting on endografts used to treat aortic aneurysms. *Stud Mechanobiol Tissue Eng Biomater.* (2011) 7:221–46. Springer. doi: 10.1007/8415_2011_73

44. Volodos SM, Sayers RD, Gostelow JP, Bell P. Factors affecting the displacement force exerted on a stent graft after AAA repair—an in vitro study. *Eur J Vasc Endovasc Surg.* (2003) 26(6):596–601. doi: 10.1016/J.EJVS.2003.08.002

45. Figueroa CA, Taylor CA, Yeh V, Chiou AJ, Zarins CK. Effect of curvature on displacement forces acting on aortic endografts: a 3-dimensional computational analysis. *J Endovasc Ther.* (2009) 16(3):284. doi: 10.1583/08-2667.1

46. Rahmani S, Grewal IS, Nabovati A, Doyle MG, Roche-Nagle G, Tse LW. Increasing angulation decreases measured aortic stent graft pullout forces. *J Vasc Surg.* (2016) 63(2):493–9. doi: 10.1016/j.jvs.2014.06.115

47. Melas N, Saratzis A, Saratzis N, Lazaridis J, Psaroulis D, Trygonis K, et al. Aortic and iliac fixation of seven endografts for abdominal-aortic aneurysm repair in an experimental model using human cadaveric aortas. *Eur J Vasc Endovasc Surg.* (2010) 40(4):429–35. doi: 10.1016/J.EJVS.2010.07.007

48. Vorp DA, Schiro BJ, Ehrlich MP, Juvonen TS, Ergin MA, Griffith BP. Effect of aneurysm on the tensile strength and biomechanical behavior of the ascending thoracic aorta. *Ann Thorac Surg.* (2003) 75(4):1210–4. doi: 10.1016/S0003-4975(02)04711-2

49. Zhu Y, Mirsadraee S, Rosendahl U, Pepper J, Xu XY. Fluid-Structure interaction simulations of repaired type A aortic dissection: a comprehensive comparison with rigid wall models. *Front Physiol.* (2022) 0:1113. doi: 10.3389/FPHYS.2022.913457

50. Ma T, Dong ZH, Wang S, Meng ZY, Chen YY, Fu WG. Computational investigation of interaction between stent graft and aorta in retrograde type A dissection after thoracic endovascular aortic repair for type B aortic dissection. *J. Vasc. Surg.* (2018) 68:14S–21S. doi: 10.1016/j.jvs.2018.06.008

51. Menichini C, Pirola S, Guo B, Fu W, Dong Z, Xu XY. High wall stress may predict the formation of stent-graft-induced new entries after thoracic endovascular aortic repair. *J Endovasc Ther.* (2018) 25:571–7. https://doi-org.iclibezp1.cc.ic.ac.uk/ 10.1177/1526602818791827 doi: 10.1177/1526602818791827

52. Singh SD, Xu XY, Pepper JR, Izgi C, Treasure T, Mohiaddin RH. Effects of aortic root motion on wall stress in the marfan aorta before and after personalised aortic root support (PEARS) surgery. *J Biomech.* (2016) 49(10):2076–84. doi: 10.1016/j.jbiomech.2016.05.011

53. Yuan X, Kan X, Xu XY, Nienaber CA. Finite element modeling to predict procedural success of thoracic endovascular aortic repair in type A aortic dissection. *JTCVS Techniques.* (2020) 4:40–7. doi: 10.1016/J.XJTC.2020.10.006

54. Kan X, Ma T, Dong Z, Xu XY. Patient-specific virtual stent-graft deployment in type B aortic dissection: a pilot study of the effect of stent-graft length. *Front Physiol.* (2021b) 20(6):2247–58. doi: 10.3389/fphys.2021.718140